Powder Technology 318 (2017) 151–161

Contents lists available at ScienceDirect

Powder Technology

journal homepage: www.elsevier.com/locate/powtec

An experimental study of the aerodynamic dispersion of loose aggregates in an accelerating flow

Nicolás Silin [a],[*], Juan Tarrio [b], Tomás Guozden [b,c]

[a] Consejo Nacional de Investigaciones Científicas y Técnicas (CONICET), Centro Atómico Bariloche, Av. Bustillo 9500, 8400 Bariloche, Argentina
[b] Instituto Balseiro, Universidad Nacional de Cuyo and Comisión Nacional de Energía Atómica, Centro Atómico Bariloche, Av. Bustillo 9500, 8400 Bariloche, Argentina
[c] Universidad Nacional de Río Negro, Mitre 630, 8400 Bariloche, Argentina

ARTICLE INFO

Article history:
Received 17 November 2016
Received in revised form 20 April 2017
Accepted 22 May 2017
Available online 24 May 2017

Keywords:
Powder dispersion
Aerodynamic
Slit
Planar jet
Powder aggregate

ABSTRACT

The dispersion of powders in gas flows is relevant in some powder processing techniques, in dry powder inhalers and in particle size analysers, among others. When using small particle sizes, the powder tends to form stronger aggregates and the dispersion becomes more difficult. There are many approaches to the dispersion process but most include collisions as one of the possible agglomerate break-up mechanisms. This is not always a satisfactory solution as particles may get contaminated or reduced. In the present work we explore the dispersion of powder aggregates in an accelerating flow with no particle-wall collisions. We built a fluid-dynamic device with a simple geometry consisting of a sharp slit, producing a rapidly converging flow at the entrance and a planar jet at the exit. A powder feeder exited with an ultrasonic actuator was used to generate single powder aggregates. The stationary flow field was calculated numerically and the velocity and degree of aggregate dispersion were assessed based on imaging results. In all the cases tested, erosion of the aggregates could be observed. In the case with the highest suction pressure, a different mechanism arises, which leads to the disintegration of the aggregate and a significantly better dispersion of the powder.

1. Introduction

Many processes involving powders require them to be suspended in a gas stream. The behaviour of the powder suspension and the outcome of the process depend on whether the particles are well dispersed or if they are part of larger aggregates. A dispersed powder suspension will have a more consistent fluid-dynamic behaviour, will stay suspended for a longer period of time and will have increased mass, heat and momentum transfer.

The dispersion process consists basically in the separation of the particles that are held together by different inter-particle forces. In general this means the application of mechanical energy to overcome these forces. There are different approaches to achieve this, depending on the powder to be dispersed and on the application constrains, a good review can be found in the work of Calvert et al. [1].

The problem of dispersing powders in gas streams is common to various applications. Industrial processes like blown powder-based deposition systems [2,3] and thermal powder processing such as the manufacturing of micro-spheres or micro-balloons require powders to be well dispersed to achieve satisfactory results [4–7]. There are even cases where a perfect dispersion is required while attrition of the particles is unacceptable, like in the seeding for particle image velocimetry [8] or in powder size analysers [9,1]. Lately the use of equipment capable of sizing powders in dry suspensions is becoming more common, with manufacturers such as Malvern, Horiba or Microtrack offering such devices. These devices present advantages when the powders to be measured are fragile, soluble, or reactive, but they usually require a careful adjustment of the operation parameters to achieve a good dispersion while keeping particle attrition at acceptable levels.

In recent years Dry Powder Inhalers (DPIs) have gathered attention as a non-invasive administration method, not only for lung specific treatments (local) but also for systemic treatments (via alveolar absorption) [10]. For the powders to reach the lungs of the patient, the dimensions of the particles have to be in the order of 3 μm or less [11,12], and have to be well diseprsed. Most DPIs rely on the patient suction power rather than using a propellant, the pressure difference and volumetric flow rate that are available to produce aggregate breakup are therefore limited. There have been numerous efforts to improve the dispersion characteristics of the powder formulations but also to assess and improve the design of the dispersers, being a very active field of research. There are many DPI devices on the market, with the majority using either turbulence or particle impaction to disperse the active pharmaceutical ingredient. However, only a few research works have focused on isolating the mechanisms of particle de-agglomeration in these devices. Most works evaluate the device efficiency, for example the fine particle dose values, for different operating conditions [13,14]. Recently,

---

[*] Corresponding author.
E-mail addresses: silin@cab.cnea.gov.ar (N. Silin), juan.tarrio@cab.cnea.gov.ar (J. Tarrio), tguozden@unrn.edu.ar (T. Guozden).

http://dx.doi.org/10.1016/j.powtec.2017.05.043
0032-5910/

Kou et al. [15] performed a microscale particle image velocimetry (PIV) study on an experimental device simulating a Rotahaler® DIP. In their study they follow the aggregates as they are dispersed by drag force, particle-particle of particle-obstacle impactions. Their study is an interesting antecedent to the present work in the sense that it aims at directly observing the mechanism of destruction of the aggregates.

Dry powder inhalers achieve dispersion mainly by promoting particle-particle or particle-wall collisions, while turbulence and other purely fluid-dynamic stresses have a minor contribution. Wong et al. [16] analysed entrainment tubes with a combined approach where computer fluid dynamics simulations were combined with experimental measurements of the output product of the device. Their results suggest that the collision of aggregates with the walls play a dominant role in the dispersion process while naturally occurring pipe turbulence had a negligible effect, apart from increasing the number of wall collisions.

Shear stress and turbulence are often mentioned as important dispersion mechanisms [1]. These mechanisms have been studied in the context of aggregation and break-up in liquid suspensions [17–19]. Saha et al. [20] used water as fluid and generated the aggregates in a simple shear flow. These aggregates were then introduced in a turbulent flow field and followed as they broke-up. Simple shear flows and turbulence are of interest for suspensions in liquids with high viscosity and density. In gas flows, on the other hand, the flow is strongly affected by the presence of the particles, which normally have a much higher density than the gas. As a result the flow field becomes much more complex, generating shear forces by the high relative velocity between the aggregate and the gas, as can also be appreciated in the results of the present work.

Dispersion devices which promote aggregate collisions, while proven effective for medical applications, may cause the attrition of fragile particles and contamination with the material of the device walls, making them less desirable for applications such as particle size analysers, or in the processing of high purity materials. In those cases dispersers based on flow acceleration or shear forces alone would be preferred. When evaluating presently used aerodynamic dispersion devices, all of them present impaction as a possible dispersion mechanism [1]. A good candidate for dispersion without impaction in gases would therefore be a fluid dynamic device capable of producing a rapid acceleration of the flow, as proposed by Sosnowski et al. [21] or by Gerde [22].

Lately the availability of very high power light emitting diodes (LEDs) and high power, high speed electronics made it possible to achieve inexpensive but high performance illumination systems. Pulsed LED illumination has been used for particle image velocimetry [23,24] and is particularly well suited for high speed shadowgraphy [25]. The availability of this technology enables us to obtain photographs of fluid-dynamic processes that occur in extremely short periods of time, as is the case of the dispersion of powder aggregates. Furthermore by using colour LEDs we can colour-code two images in a single RGB (red-green-blue) image, making velocity estimations also possible [26].

The present study is therefore aimed at improving the understanding of the mechanisms of particle de-agglomeration produced by flow acceleration alone. We expect the acceleration of the flow to produce normal and shear stresses on the aggregate that will eventually erode or break-up into smaller aggregates or individual particles. In the present study the dispersion device was designed in such a way that impaction with the device walls is eliminated as a possible dispersion mechanism and turbulence is absent in the region of interest. The flow was also modelled numerically to obtain the velocity field. This imposed the requirement of having a flow that was well suited for numerical modelling. For this purpose we have chosen a suction slit formed between two sharp edges. High speed photography based on pulsed LED illumination was used to obtain images of the agglomerates and to estimate their velocities and sizes at different positions in the fluid-dynamic device. These measurements allow estimating the type of dispersion mechanism that is involved, either erosion or break-up in smaller aggregates, and the conditions at which these occur.

2. Experimental method

The objective of the experimental device is to capture two successive images of a single breaking aggregate. The overall scheme of the measurement system is shown in Fig. 1. The powder aggregate is produced by the powder feeder and falls into the fluid-dynamic device that will

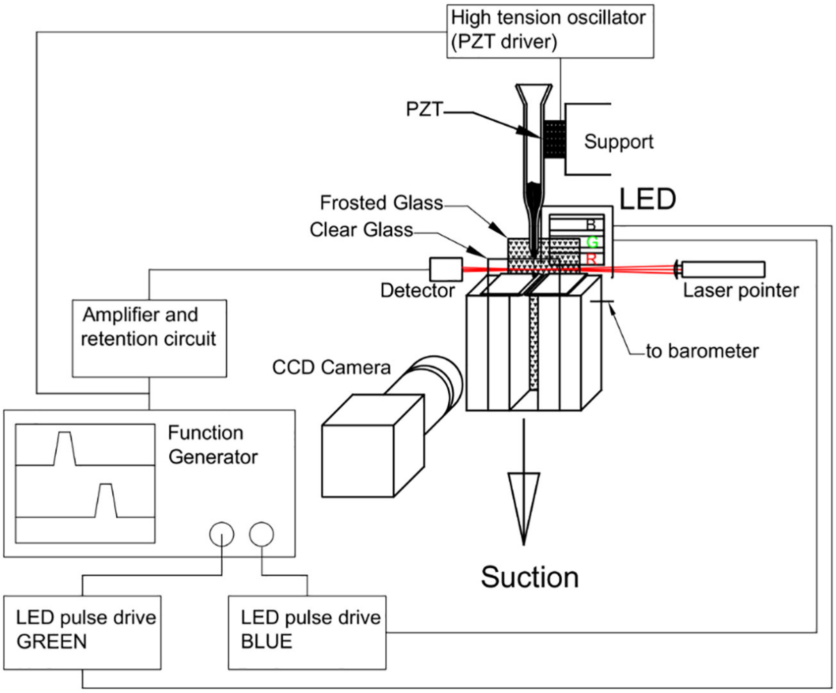

Fig. 1. Scheme of the experimental device. The light pipe between LED and the frosted glass was omitted for clarity.

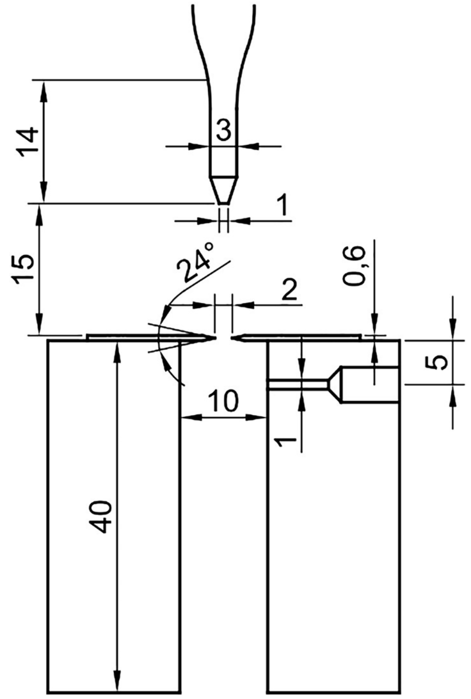

Fig. 2. Dimensions of the fluid dynamic device and powder feeder.

cause the dispersion. A colour CCD camera is used to capture the shadow image of the aggregate, which is illuminated from the back by a fast pulsed LED lighting system. There are two illumination pulses, a green pulse followed by a blue pulse, thus producing two images per event, one in the green field and one in the blue field of the colour image. To capture the precise moment where the particle is in transit, a barrier type switch, made with a continuous laser diode and a photo-detector, is used to trigger the LED illumination.

The fluid-dynamic device is a horizontal slit with suction on the lower side. The purpose of this device is to generate a 2D flow with a central region where high acceleration is produced. The flow can be separated in two zones, a flow intake into the slit and a planar exit jet. The intake presents strong favourable pressure gradients and behaves as a potential flow with negligible boundary layers, as will be discussed later. Planar jets, on the other hand, have been thoroughly studied for their implications in flow stability and for their technological interest and are very well characterized [27–30]. This planar set-up is also convenient for visualization as it presents good optical access.

The depth of field of the imaging system is in the order of 0.5 mm. To obtain clear images of the aggregates they have to be introduced individually and at the same position every time. This is rather difficult with pre-formed spherical aggregates as they tend to break when manipulated. We opted to produce the aggregates in-situ by means of a vibrating capillary tube. Lu et al. [31] studied different powder feeders and found that under certain conditions; cohesive powders in a capillary tube exited with ultrasonic vibrations tend to flow discontinuously, forming cylindrical aggregates. Here we have taken advantage of this behaviour to produce a regular supply of cylindrical aggregates. The diameter of the aggregates is determined by the internal diameter of the capillary tube, which is (670 ± 15) μm. The length of the aggregate depends on the cohesiveness of the powder [31], but in our case it was between 0.5 and 1 mm long. To produce the ultrasonic vibration of the capillary tube we used a piezoelectric actuator directly attached to the glass capillary tube, as shown in Fig. 1. The piezoelectric actuator was driven by a 300 V (peak to peak) oscillator based on the IR2153 self-oscillating half-bridge driver. The frequency was tuned to one of the natural frequencies of the capillary tube, approximately 31 kHz.

The scheme and dimensions of the device are shown in Fig. 2. The device has two parallel acrylic blocks 10 mm apart, and two glass walls at the front and at the back, forming a rectangular channel. The distance between the glass walls is (20 ± 0.5) mm. On top of the acrylic blocks there are two 18 mm snap-off blades, cut in length to fit snugly in the space between the glass walls. The (2 ± 0.05) mm separation between the blades forms the slit. The glass walls at the front and at the back of the device continue upwards to obtain an almost two dimensional flow field. The capillary tube that supplies the powder aggregates is placed (15 ± 0.5) mm above the slit and is tapered to minimize the wake that is introduced in the flow. At 5 mm below the slit, on the depression side of the device, there is a pressure tap that is used to measure the working depression which in turn is used to calculate the reference air velocity.

2.1. Test conditions

The test conditions are detailed in Table 1. In all conditions the atmospheric pressure stayed approximately constant and we increased the suction depression by approximately double each time. The reference velocity V_{ref} is the maximum possible velocity in the fluid-dynamic device and is calculated based on the atmospheric pressure P_0, temperature T_0 and suction pressure P_{suc}, and applying the compressible flow relations for subsonic conditions [32]:

$$Ma_{ref} = \sqrt{\frac{2}{k-1}\left(\left(\frac{P_0}{P_{suc}}\right)^{(k-1)/k} - 1\right)}, \quad (1)$$

$$T_{ref} = T_0\left(1 - \frac{k-1}{2} Ma_{ref}^2\right)^{-1}, \quad (2)$$

$$V_{ref} = Ma_{ref}\sqrt{kRT_{ref}}, \quad (3)$$

where k is the specific heat ratio, R is the air gas constant, Ma_{ref} the reference Mach number and T_{ref} the reference temperature.

2.2. Imaging setup

The imaging system is composed of a colour CCD camera connected to a PC, and an RGB LED module that produces two light pulses, a green pulse followed by a blue pulse. The pulse separation was varied for each case in order to obtain a satisfactory estimation of the aggregate speed. The production of powder aggregates is a very stochastic process and the wait time between successive occurrences is variable. On the other hand this wait time is several orders of magnitude longer than the characteristic time of the dispersion process. It was therefore necessary to use a detector to trigger the image capture, but also to avoid two

Table 1
Test conditions.

	Atmospheric pressure (kPa)	Suction side pressure (kPa)	Pressure difference (kPa)	Reference velocity V_{ref} (m/s)	Pulse separation τ_p (μs)
Case 1	92.06 ± 0.02	91.25 ± 0.03	0.81 ± 0.04	39 ± 2	300
Case 2	92.06 ± 0.02	90.33 ± 0.10	1.73 ± 0.10	56 ± 2	200
Case 3	92.04 ± 0.02	88.04 ± 0.3	4.0 ± 0.3	86 ± 3	100
Case 4	92.03 ± 0.02	82.33 ± 0.5	9.7 ± 0.5	136 ± 4	70

separate occurrences to be recorded on the same image. The trigger is an inexpensive laser pointer focused on the plane that crosses the aggregate trajectory, at approximately 5 mm over the slit (see Fig. 1). The laser light is then detected by a photo-transistor and the signal amplified by an operational amplifier. When the laser beam is interrupted the operational amplifier outputs a step signal. This signal is locked by a retention circuit that prescribes the occurrence of a second trigger and disconnects the piezoelectric driver to avoid wasting powder. The trigger signal starts a function generator (Siglent SDG1050) where pulse duration, separation between pulses and pulse delay with respect to the trigger signal are set. These signals control the drivers for the green and blue LEDs. The details of the driver design are explained in the work of Willert et al. [33]. In the present case we have replaced the MOSFET transistor by the CSD18542KTT and the driver by the UCC27511DBVR, both manufactured by Texas Instruments. These replacements provide faster response than the original components and allow shorter illumination pulses. Illumination pulses used in the present study have duration of approximately 600 ns for each colour, green and blue respectively, and a pulse separation that was varied according to the phenomenon velocity.

The light emitted by the RGB LED is too uneven to be suited for shadow photography and the use of a simple light diffuser made with a frosted glass did not provide a satisfactory illumination. This problem was previously discussed by Susa [34]. In the present set-up we introduced a light pipe between the LED and the light diffuser. The light pipe used was built with four front surface mirrors, making it 25 mm high, 25 mm wide and 90 mm long. It was noticed that the use of the light pipe also reduced the image noise as compared to the light diffuser alone. To verify the performance of the illumination system we measured the light pulse output with a sensor based on an avalanche photodiode. The sensor output is shown in Fig. 3, where the pulse separation was reduced to fit both pulses in the same image. The duration of the pulses results from a compromise between illumination energy per pulse and the blur produced by particles moving during each illumination pulse.

2.3. Characterization of the powder and powder aggregates

To produce the aggregates we looked for a powder that, while being cohesive, had a simple chemical composition and could be readily purchased. We chose irregularly shaped aluminium oxide powder supplied by Sigma Aldrich. We have measured the particle size distribution with a Microplus Mastersizer particle size analyser. The results are shown in Fig. 4 and show the measured powder size range is from 4 μm to 20 μm.

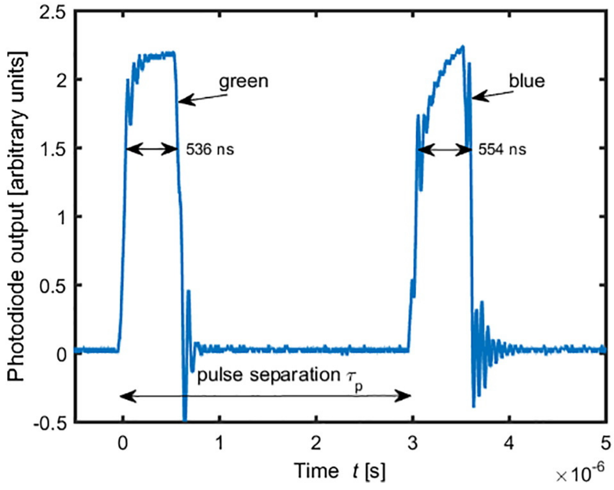

Fig. 3. Illumination pulses as measured by a fast avalanche photodiode sensor.

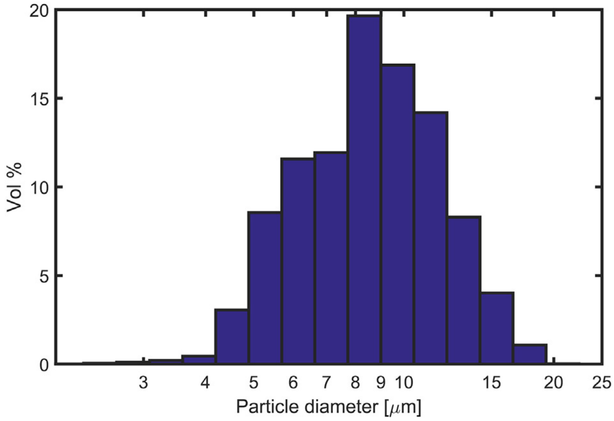

Fig. 4. Particle size distribution of used powder.

The particle morphology can be observed in the micrograph shown in Fig. 5 (Scanning Electron Microscope). The aerated density was estimated by sieving the powder trough a 75 μm mesh and pouring it into a graduated cylinder to measure the volume. Then the cylinder was taped in a taping device and finally the powder was weighed. The aerated density resulted (1.08 ± 0.05) g/ml and the tapped density (1.69 ± 0.03) g/ml, giving a Carr index of 36.

To produce the aggregates the powder is fed by a vibrating capillary tube. This produces the compaction of the powder, resulting in certain strength of the agglomerate. It is not possible to estimate the strength of the agglomerate from the bulk properties of the powder alone. In general the mechanical resistance of a powder is dependent on its stress and strain history [35]. In the present case we developed a simple device to measure the force necessary to produce the failure of the aggregate. In this device the cylindrical aggregate is tugged laterally by means of a fine stainless steel wire, (0.10 ± 0.01) mm in diameter and approximately 15 cm long (Fig. 5). The elastic constant of the wire was first calibrated by hanging small aluminium foil pieces of known weight from the wire tip and measuring the displacement. A series of agglomerates were deposited on a flat glass by means of the vibrated capillary tube. Then, using a micrometric screw and watching through a magnifying glass, the wire tip was laterally approximated to one aggregate. By further advancing the micrometric screw the wire was bent elastically by

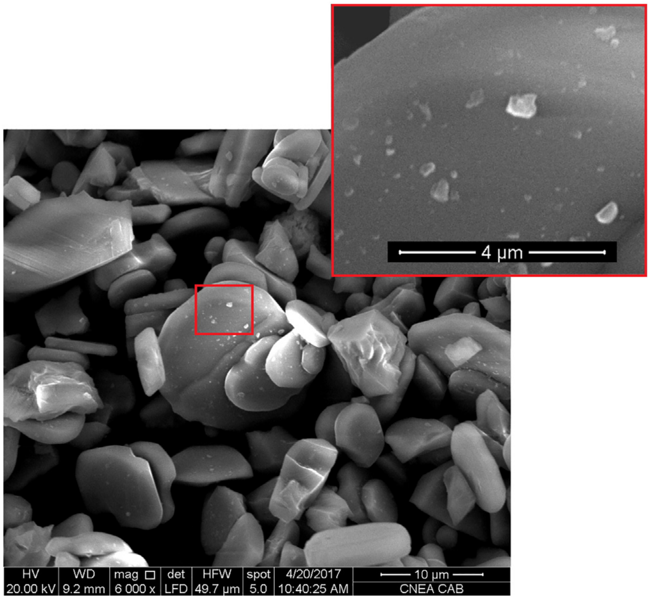

Fig. 5. Scanning electron micrographs of the powder. The lower scale bar is 10 μm and the upper one in the zooming picture is 4 μm.

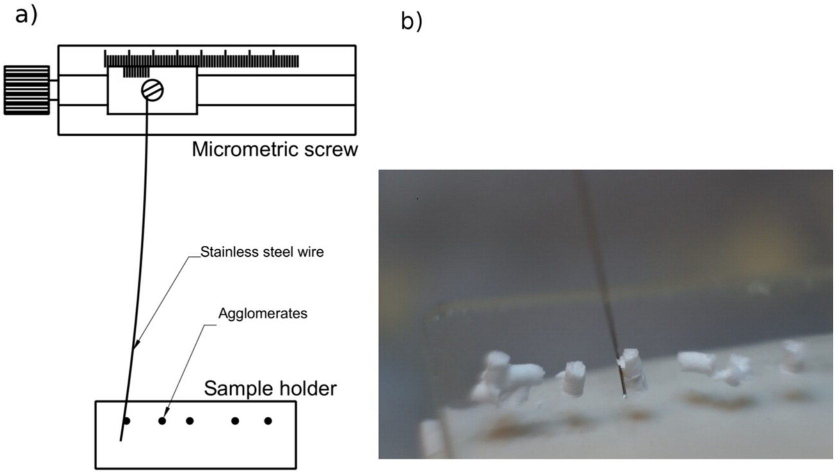

Fig. 6. Aggregate resistance tester: a) Top view scheme of the device, b) Photograph of aggregate being tested.

forcing it against the cylindrical aggregate until it failed. The force exerted was estimated from the micrometric screw displacement from the contact point up to the aggregate failure. In Fig. 6 we show several powder aggregates and the wire in contact with one of them during a test.

The result from this test is shown in Fig. 7. The radial failure shear stress σ_e is calculated as:

$$\sigma_e = \frac{F_e}{\frac{\pi}{4} d_{Agg}^2}, \tag{4}$$

where F_e is the radial failure shear force measured and d_{Agg} is the aggregate diameter. The results show the radial failure shear stress has a median value of 12 Pa and a standard deviation of 6 Pa.

As an order of magnitude verification of these results we propose the cylindrical aggregate breaks away from the powder feeder when the weight of the hanging cylinder divided by the traverse area S_{Agg} reaches the detachment stress $\sigma_{d,}$

$$\sigma_d = \frac{\rho_{Agg} g Vol_{Agg}}{S_{Agg}} = \frac{\rho_{Agg} g \frac{\pi}{4} d_{Agg}^2 h}{\frac{\pi}{4} d_{Agg}^2} = \rho_{Agg} g h, \tag{5}$$

where ρ_{Agg} is the aggregate density, g the acceleration of gravity, Vol_{Agg} the volume of the aggregate, and h the aggregate length. For an aggregate length of 1 mm we get a detachment stress value of 16.6 Pa which is in good agreement with the radial failure shear stress test results.

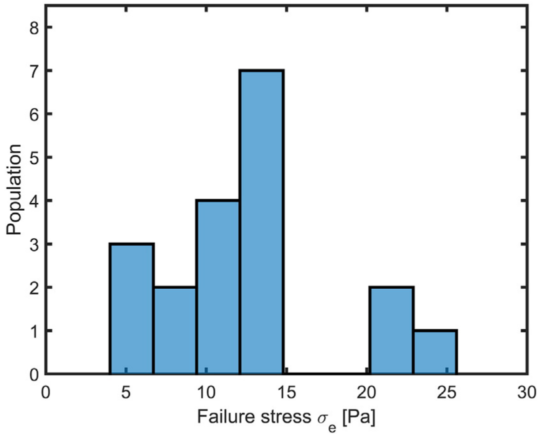

Fig. 7. Radial failure shear stress of individual agglomerates.

These values should be regarded as approximate and give an order of magnitude estimation of the aggregate resistance. Also the failure shear stress along other planes will differ, as the powder is compressed radially and stretched axially in the capillary tube, making the aggregate anisotropic.

2.4. Image processing

With the present approach two consecutive instants can be captured separately in the green and blue channels of the camera. Because of the great number of available images, automated methods where developed for processing the images and inferring the characteristics of the powder, in particular two measures were of interest: front position and powder cloud dimensions. The image processing pipeline is divided in three stages: image pre-processing, front position measurement and cloud size estimation.

2.4.1. Image pre-processing

In this stage the channels are split and inverted, in order to show the powder cloud in brighter intensity. Then a background image is subtracted to clear lighting artefacts and the slit image.

Because of the overlapped spectral response of the different colour filters, inter-channel interference appears in the two channels. If this process is modelled to be additive, the effect can be reduced by applying a pixel-wise linear transformation to the green and blue channels as discussed in the work of McPhail et al. [36]. The parameters of this linear transformation where manually tuned to accomplish the desired demuxing. Fig. 8 shows the original image and the pre-processing output at different steps, for a typical picture.

2.4.2. Front position estimation

In order to estimate front position, in each of the channels, we calculate the sum of the pixels over each row of the image:

$$S(y) = \sum_x I(x, y) \tag{6}$$

where I(x,y) is the image intensity field. Fig. 9 shows S(y) and it's smoothed numerical derivative. The front position is estimated by looking at the peak in the derivative function and then refined by searching back until a certain percent of the peak amplitude is reached. We chose a value of 10% for the present image series.

It is important to note that this algorithm proved independent of the powder cloud shape, which changes substantially from picture to

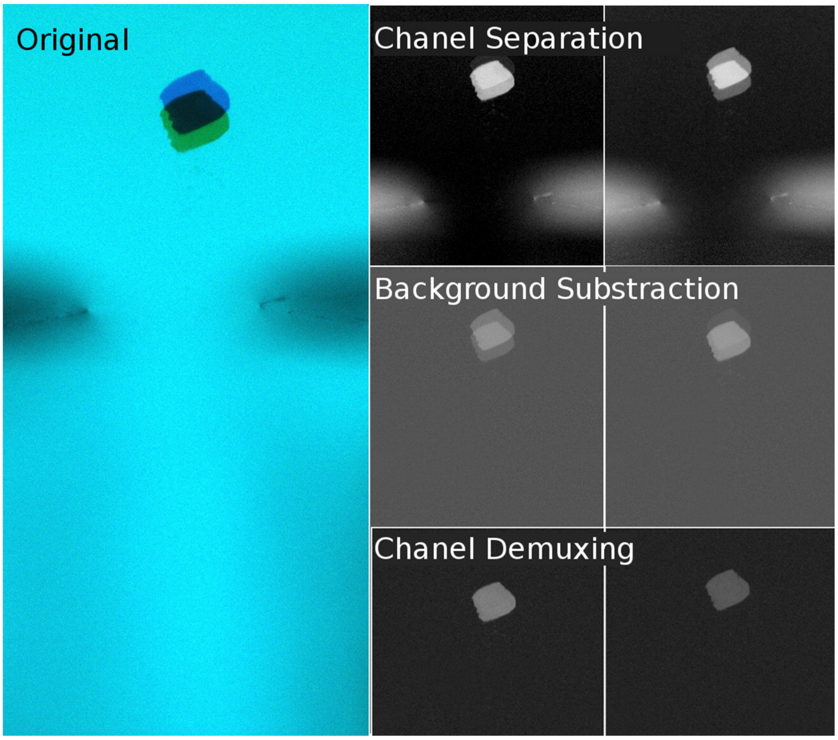

Fig. 8. Image pre-processing: Channel separation, background subtraction and channel demuxing.

picture. Its integral characteristic makes it robust against noisy and cloudy situations, like the one show in Fig. 10b).

2.4.3. Cloud size estimation

In order to estimate cloud size an integral robust measure was required, in particular we chose the intensity weighted second moment of area in both vertical and horizontal axes. In order to increase precision, the images were pre-masked by comparing their local mean intensity with the mode of the intensity of the whole image, determined by calculating an intensity histogram. This mode intensity is also subtracted from the selected regions, in order to reduce the effect of noisy local zones whose mean intensity is close to the mode but still within the mask.

In Fig. 10 we present the output of the image processing for two cases, the "easy" case showed in a), where the shape is well defined, and a "hard" case in b), where the powder is very cloudy and undefined. The calculated sizes are represented by ellipses with the corresponding horizontal and vertical sizes. It can be seen how in both cases the algorithms yield satisfactory results.

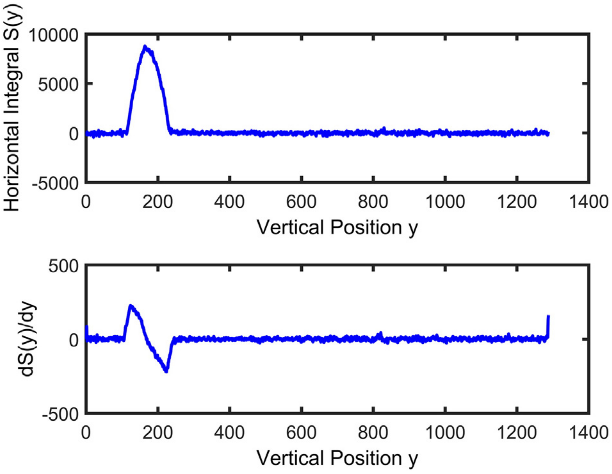

Fig. 9. Image processing to obtain the cloud front position.

3. Numerical simulation of the flow field

The flow in the experimental device was modelled using Fluent simulation software. For the simulations we considered a 2D section of the fluid-dynamic device and we applied symmetry conditions along the vertical symmetry plane to model one half of the flow field. We used

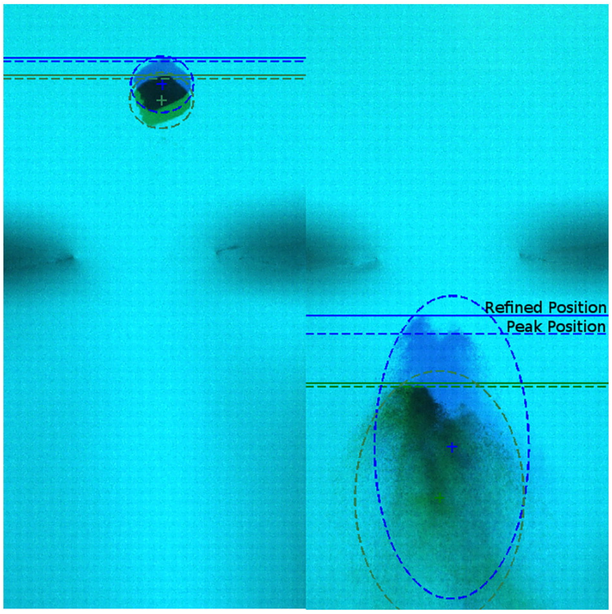

Fig. 10. Examples of front position and size estimation results. a) Agglomerate with no degradation b) Disintegrated agglomerate.

Table 2
Mesh parameters and resulting mass flow rate.

Mesh	1	2	3	4
Number of elements	4750	19,000	76,000	304,000
Max. aspect ratio	2.54	2.49	2.53	2.55
Min. orthogonal quality	0.79	0.79	0.79	0.79
Mass flow rate (case 4) [kg/(s m)]	0.08609	0.08672	0.08717	0.08767

the pressure-based solver and we obtained the steady state solution. The simulation domain was extended 15 mm upstream from the slit position to reach the position where the powder feeder is located. We chose pressure boundary conditions for both inlet and outlet. Turbulence was introduced by the Spalart-Almaras model, but it is negligible in the imaging region. Air properties were taken as constant: 28.97 g/mol for molecular mass, 1.7894 e-5 kg/(m s) for viscosity, 1006.43 J/(kg K) for specific heat (Cp) and 0.0242 W/(m K) for thermal conductivity.

The mesh was refined in the neighbourhood of the slit edges, resulting in an initial mesh of 4750 quadrilaterals. This mesh was subsequently refined dividing each quadrilateral into four new quadrilaterals, to ensure numerical convergence. The minimum orthogonal quality and the maximum aspect ratio of the meshes are also shown in Table 2. The largest effect of increasing the mesh resolution is a reduction in the thickness of the boundary layers, the profiles of pressure and velocity in the symmetry axis showed acceptable convergence already in the second refinement.

The velocity magnitude field for Case 4 is shown in Fig. 11. It can be noted that at 15 mm above the slit the air velocity is negligible. It can also be observed that if the aggregate falls within a range of 0.5 mm from the vertical symmetry line it will experience very small lateral velocity gradients. Vertical velocity gradients are concentrated in the neighbourhood of the slit, as expected.

In Fig. 12 we show the vorticity magnitude for the mean velocity flow field for Case 4. Here the vorticity magnitude is calculated as:

$$|\omega| = |dV_y/dx - dV_x/dy| \tag{7}$$

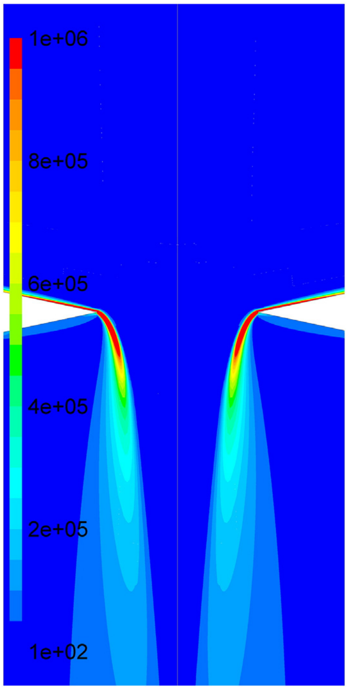

Fig. 12. Contours of vorticity magnitude for Case 4 as calculated by Fluent. Vorticity values are presented in 1/s.

where V_y is the mean velocity component in the y direction and V_x is the mean velocity component in the x direction of the flow. It is clear that the flow area traversed by the aggregate is approximately irrotational while the vorticity is concentrated in the boundary layers and in the periphery of the area of interest.

In Fig. 13 we can see the velocity along the vertical symmetry line for each of the cases. The velocities are presented in non-dimensional form scaled by the reference velocity V_{ref}. It can be seen that all the velocity profiles are similar and scale very well with V_{ref}.

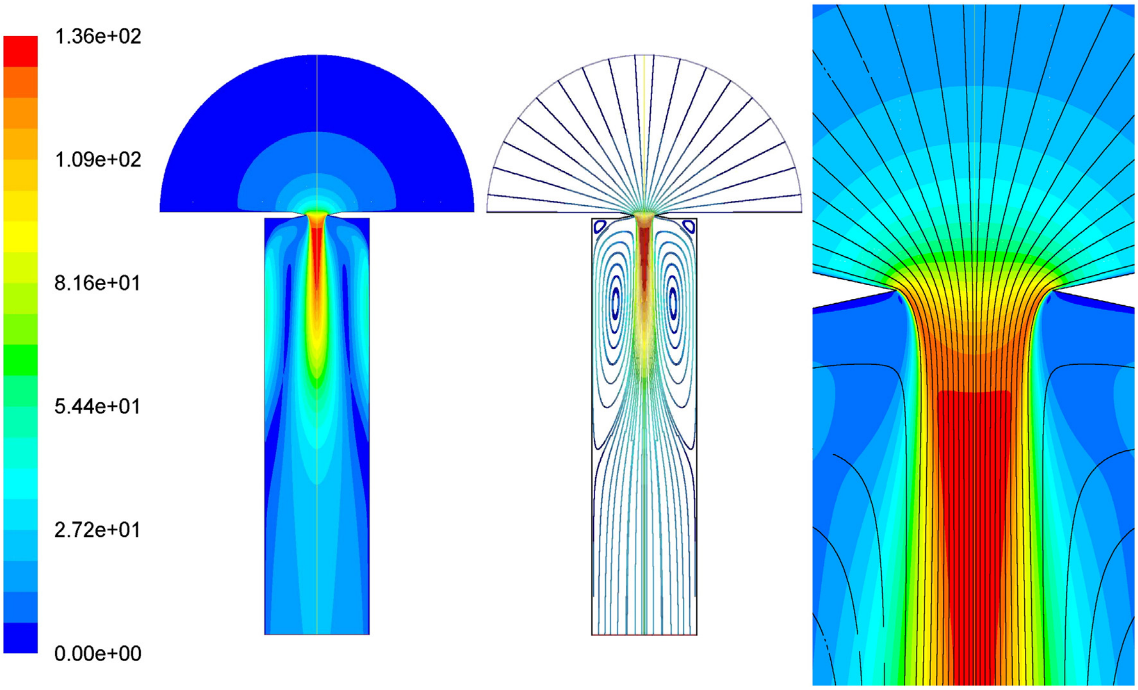

Fig. 11. Contours of velocity magnitude (left), pathlines (centre) and a detail of the imaging section (right) for Case 4 as calculated by Fluent. Velocities are presented in m/s.

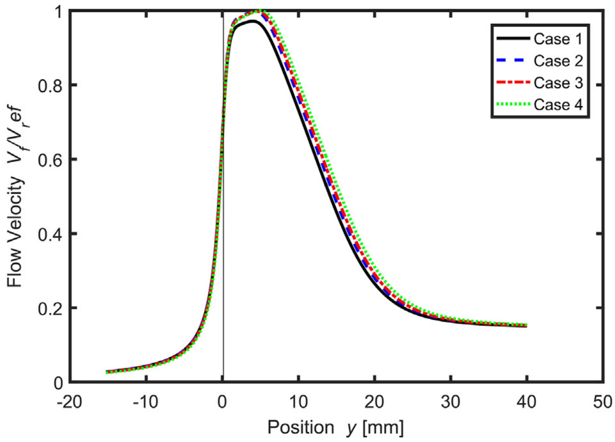

Fig. 13. Velocity profiles along the vertical symmetry line. Values are presented non dimensionalized by the reference velocity.

In Fig. 14 we show the pressure profile along the vertical symmetry line. The pressure falls as the flow accelerates with the highest pressure gradients at the slit. There is also a small pressure recovery downstream because of the jet expansion. It is worth noting that we are not interested in aggregates that transit the slit too close to the edges and we will limit the study to particles that are well centred respect to the slit.

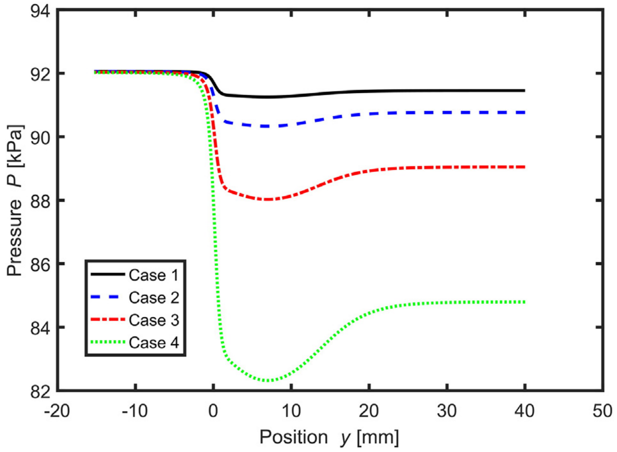

Fig. 14. Pressure profiles along the vertical symmetry line.

4. Results

The generation of the aggregates is a very variable process, the periodicity, the length of the aggregates as well as the precise falling position may vary between events. In Figs. 15 and 16 we present a selection of images of aggregates at different positions: at approximately 2 mm above the slit, at the slit and below the slit. For this purpose we have taken the blue colour field alone and pre-processed the images as described above. The two wedges indicate the position of the slit for reference.

In Fig. 15 we see images corresponding to Case 1. We can observe that the size of the incoming aggregate can be very variable. We can observe some chipping of the aggregates in Fig. 15a) followed by an erosion process in b) and c), but in most of the cases the aggregates reach the lower end of the window with their original diameter or a significant fraction still agglomerated.

In Fig. 16 we present a selection of images for Case 4. In this case larger agglomerates tend to break before arriving to the slit and all of the cases show total disintegration after crossing the slit. It is also interesting to note that all of the agglomerates show break-up and that the process is not limited to erosion.

We have observed that the behaviour of the aggregates has a large dispersion; we have therefore collected approximately 200 images per case and calculated the position of the centre of mass, the front vertical speed, and the vertical and horizontal sizes of the powder clouds. In Fig. 17 we see the agglomerates front vertical speed V, non-dimensionalized by the reference speed V_{ref}. It is interesting to note that when scaling the results by means of V_{ref} we obtain very good grouping of the lowest velocities for the different cases.

We can see that the velocity of the aggregates is much smaller than the air flow velocity calculated numerically (Fig. 17). The contribution of gravity is only significant for Case 1, causing a maximum velocity increase in the order of 20%, while it is negligible for the other cases.

For Case 1 all the events are grouped around the line of lowest velocities. The other cases show a similar behaviour except for Case 4, which has a significantly larger velocity scatter. It is also interesting to note that for the furthest downstream positions measured ($x > 2.5\ mm$), the scaled velocities for Case 4 are higher than for the other cases.

In Fig. 18 we see the results for the horizontal size of the powder cloud L_y as a function of vertical position of the centre of mass of the image. In the figure we have indicated the size of the powder feeder hole, i.e. 670 μm, and the position of the slit, $x = 0$. For Case 1 to 3 there are many measurements on the 670 μm line. Because of the flow contraction above the slit, there are slightly less large powder clouds close to the slit position. Downstream from the slit, aggregates tend to erode and expand laterally, but still for Case 1 and Case 2 there is a large number of powder clouds with small sizes for the furthest positions. This is in contrast with Case 3 and Case 4 that show almost

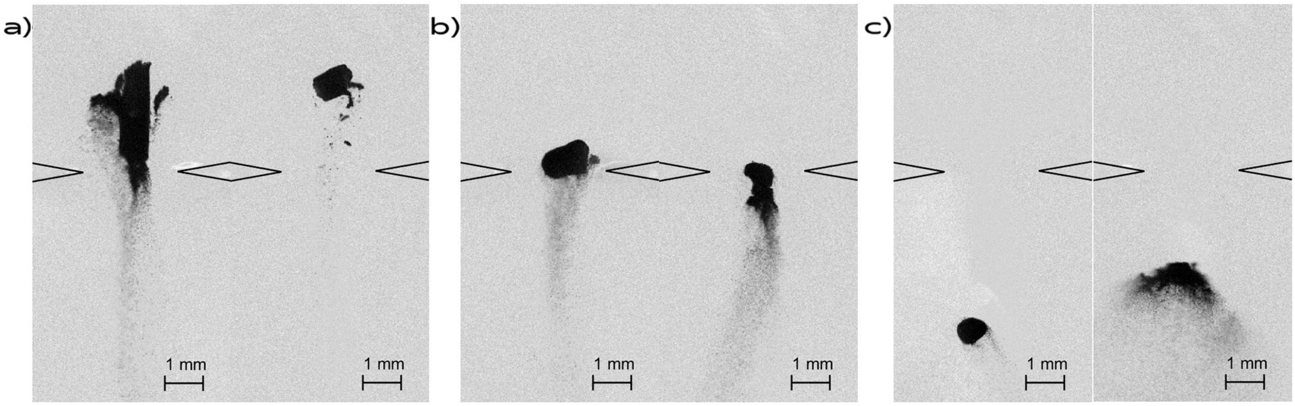

Fig. 15. Photographs of agglomerates for Case 1: a) above the slit, b) at the slit, c) passed the slit.

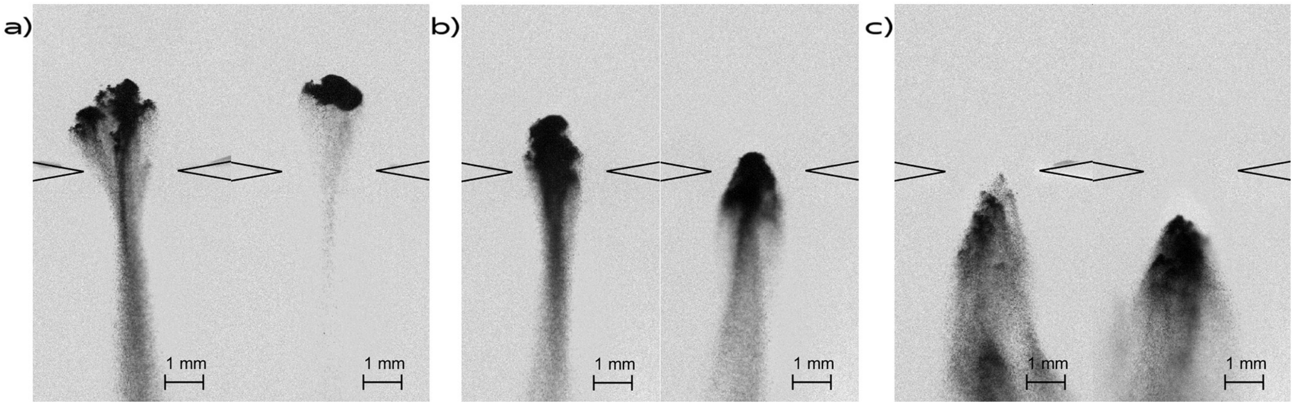

Fig. 16. Photographs of agglomerates for Case 4: a) above the slit, b) at the slit, c) passed the slit.

exclusively larger sizes. Case 4 has a different behaviour from the other cases, with lateral sizes increasing sooner, before arriving to the slit.

When the aggregates suffer erosion they produce a long tail that resembles a comet, as shown in Fig. 15 and more dramatically in Fig. 16. To have a measure of the erosion damage on the aggregate we calculated the vertical size of the powder cloud. The results are presented in Fig. 19. It should be noted here that the finite size of the images that are being processed limit the size of the observed powder clouds as they move further downstream. This causes the measured sizes to fall to zero at *x ~ 4 mm*. For Case 1 to 3 the vertical size increases only moderately upstream from the slit and more pronouncedly downstream. In comparison, Case 4 shows a much earlier increase in size. Overall it can be said that all cases show erosion of the aggregates with very few cases remaining within the minimum diameter.

5. Discussion

From Fig. 17 we see that the velocity of the aggregates is, in most of the cases, negligible respect to the velocity of the air flow. The events with lower velocities are well grouped, while the occurrence of higher velocity events increases significantly for Case 4. An aggregate that is more dispersed will have a higher area exposed to the flow being subject to higher overall drag forces. Dispersed aggregates will therefore suffer a higher acceleration and, with time, reach higher velocities. The higher velocity events of Case 4 indicate not only better dispersion but also sooner dispersion of the aggregates. If we focus at the furthest downstream positions, for Case 4 there are almost no events along the minimum velocity line, while for Case 1 and Case 2 most of the events are grouped at the lowest velocities.

If we observe the vertical size, i.e. the streamwise size of the powder clouds in Fig. 19, it is clear that only a few events show a size comparable with the original aggregate size, most observations show an increased size. This correlates with the observation of aggregate erosion in almost all the images obtained. Erosion is related to the shear tensions generated on the external layers of the aggregate by the velocity difference with the flow. In Fig. 20 we present a histogram of the vertical sizes of all events grouped by case and normalized by the total number of measurements. While from Case 1 to Case 3 they show a similar distribution, Case 4 shows a qualitative difference, with predominance of larger sizes. This change of behaviour is due to the disintegration of the aggregates before they arrive to the slit, as can be observed in Fig. 16a).

The aggregates that disintegrate show a larger horizontal size. To compare the phenomenon of aggregate disintegration for the different cases we present in Fig. 21 the histogram of horizontal sizes for all events with centre of mass upstream of the slit. In this figure also Case 4 shows a differentiated behaviour respect to the other cases, with a

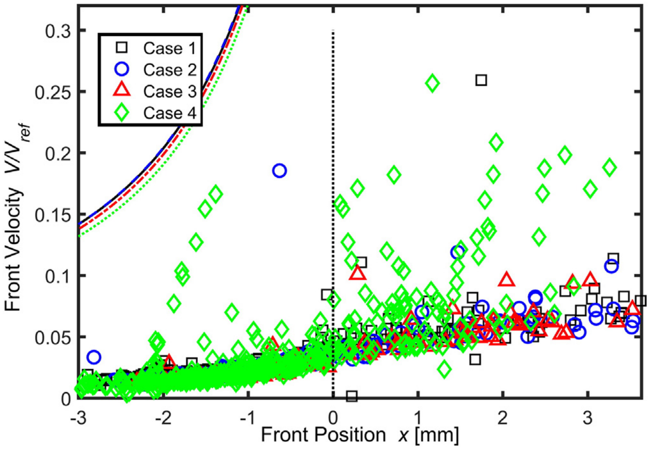

Fig. 17. Aggregate upper edge velocity as function of position. Lines show the air velocity as calculated by numerical simulation without powder. For reference see Fig. 13.

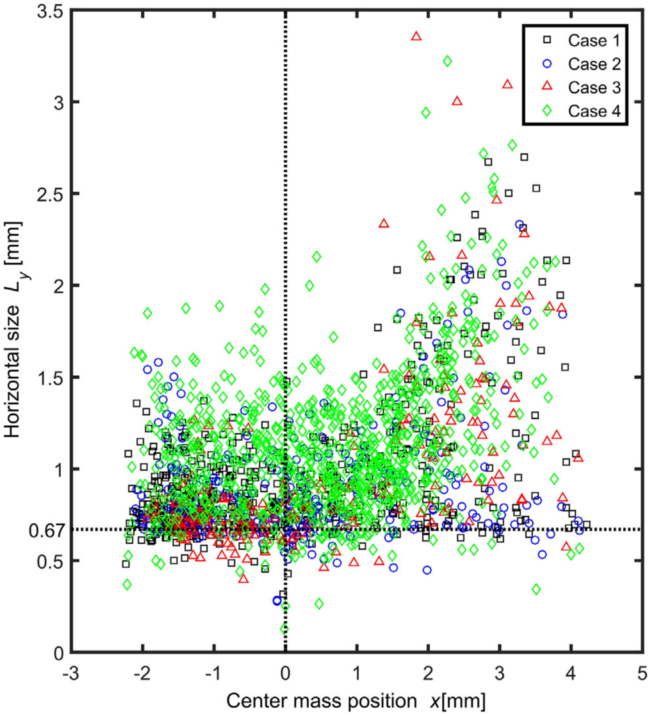

Fig. 18. Horizontal size of the powder cloud as a function of the position of the centre of mass.

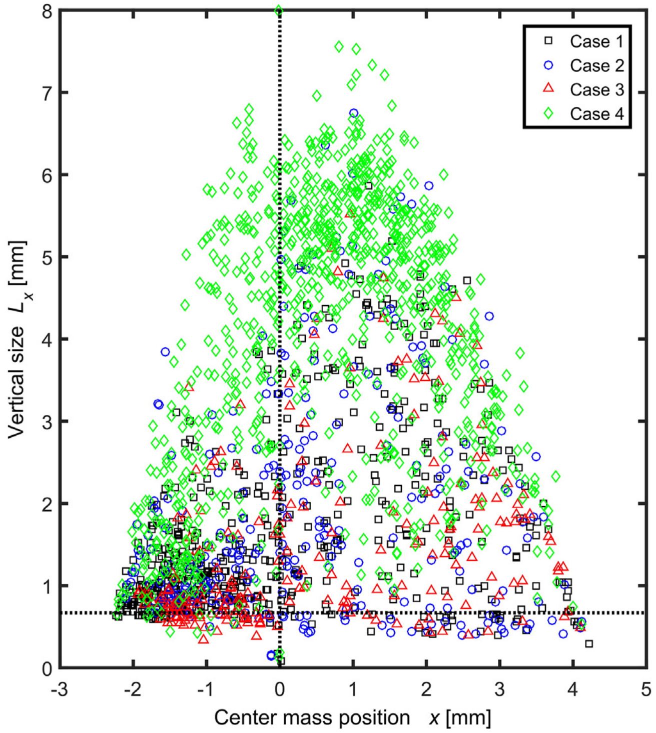

Fig. 19. Vertical size of the powder cloud as a function of the position of the centre of mass.

clear increase of the horizontal aggregate size. It is interesting to note that Case 3 has a narrower size distribution with a significant number of events that have a smaller horizontal size.

It can be concluded that Case 4 shows a distinct behaviour from the other cases, which cannot be regarded as an incremental change but rather the triggering of a different process that occurs in the flow contraction upstream from the slit. This is in qualitative agreement with the observations of Calvert et al. [37], for spherical aggregates accelerated in a uniform flow field. Calvert et al. applied the distinct element method coupled with a continuum model for the fluid phase to simulate fluid–solid interaction. He observed two dispersion modes. The first mode was observed in an aggregate exposed to high air velocities, showing rapid disintegration into individual particles. The second mode, observed in larger aggregates exposed to lower air velocities, was erosion of the external layers. In the present study the aggregates are composed of a large number of particles and therefore we observe erosion in all the cases. In Case 4, with the highest driving pressure difference, we reach a condition in which the aggregate disintegrates. It seems that larger drag forces are required to achieve complete aggregate disintegration. On the other hand sudden depressurization of the aggregate could also work as a mechanism of instantaneous disintegration. This would also be a realistic case for the instantaneous disintegration hypothesis used by Weiler et al. [38]. As the aggregate transits through the slit, it sees its surrounding pressure drop rapidly from atmospheric down to the suction pressure. Even for Case 1 the pressure drop is 810 Pa, much larger than the failure shear stress, approximately 12 Pa. If we think about the air contained in the spaces between the particles of the aggregate, it will escape between the particles, but it will also generate a tensile stress on the agglomerate. The fact that for Case 1 some aggregates of significant size make it through the fluid-dynamic device is remarkable and deserves further study.

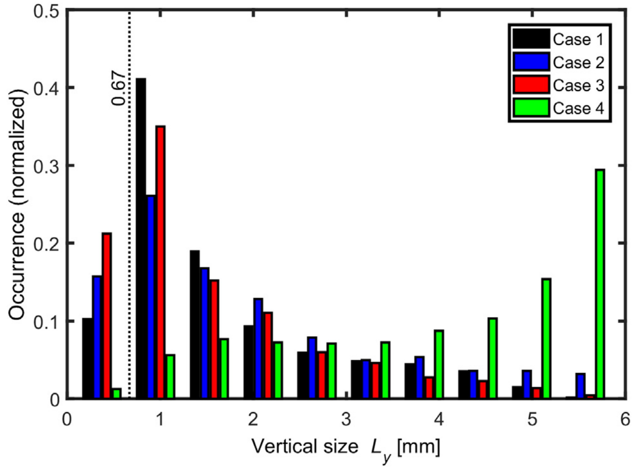

Fig. 20. Vertical size distribution of all the observed powder clouds.

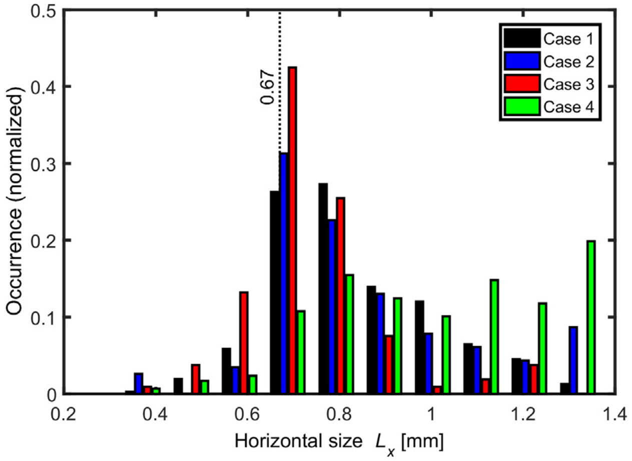

Fig. 21. Horizontal size distribution for powder clouds with the centre of mass upstream from the slit.

During the development of the experimental work, and later during the analysis of the images obtained, it became clear that having cylindrical aggregates makes the interpretation of the results more difficult, as they tend to depart from the perfectly vertical position, acquiring different yaw angles. Also, while the powder feeder designed for the present study has proven effective in producing adequate agglomerates and introducing them conveniently in the flow, the lack of control over the length of the agglomerates and the agglomerate cylindrical shape, proved to be a disadvantage. It is likely that to obtain higher quality experimental data a set-up capable of supplying spherical aggregates would be needed.

6. Conclusions

To the best of our knowledge, the dispersion of loose powder aggregates by an accelerating flow without particle-obstacle collisions was observed directly for the first time. The loose aggregates were produced by a vibrating glass capillary tube directly above the fluid-dynamic device that produces the flow acceleration.

The powder used is high purity Alumina with a size range of 5 μm to 20 μm. As the strength of the aggregates is likely to depend on its stress and deformation history, we decided to carry out an approximate measurement by means of an *ad hock* shear test. The results show an aggregate radial failure shear stress with a median value of (12 ± 6) Pa. It is remarkable that even for the study Case 1 a significant portion of the agglomerates made it through the fluid-dynamic device without disintegration. In this case the flow driving pressure difference is 810 Pa, approximately 40 times the failure shear stress of the aggregate. This also implies that this type of flow is only capable of dispersing loose aggregates, while for stronger aggregates a different dispersion mechanism would probably be required.

We found that there are two distinct dispersion processes, that where already reported in previous works [37]. For Cases 1, 2 and 3 the main dispersion mechanism is erosion, possibly followed by disintegration. Yet for Case 4 it has been observed that large part of the aggregates disintegrate before arriving to the slit. This happens at a position where the aggregate finds high velocities but also very high flow strain rates and pressure gradients. These observations are in agreement with the conclusions of the work of Calbert et al. [39] but demonstrate that disintegration is still possible for an aggregate with a large particle count if the generated forces are further increased.

Acknowledgements

The authors wish to express their recognition to Gustavo Sepúlveda, Jorge R. Issa, Enrique Aburto, Matías Isla, Silvina Pérez Fornells, Afra Fernandez Zuvich, Mora Soldati and to the members of the electronics department of the Centro Atómico Bariloche that helped with different aspects of the experimental work. This work was funded by a research project from Agencia Nacional de Promocion Científica y Tecnologica of Argentina [project PICT 2013-1404].

References

[1] G. Calvert, M. Ghadiri, R. Tweedie, Aerodynamic dispersion of cohesive powders: a review of understanding and technology, Adv. Powder Technol. 20 (1) (2009) 4–16.

[2] A.J. Pinkerton, L. Li, Direct additive laser manufacturing using gas-and water-atomised H13 tool steel powders, Int. J. Adv. Manuf. Technol. 25 (5-6) (2005) 471–479.

[3] H. Tan, F. Zhang, R. Wen, J. Chen, W. Huang, Experiment study of powder flow feed behavior of laser solid forming, Opt. Lasers Eng. 50 (3) (2012) 391–398.

[4] G.J. Ehrhardt, D.E. Day, Therapeutic use of 90Y microspheres, Int. J. Radiat. Appl. Inst. B Nucl. Med. Biol. 14 (3) (1987) 233–242.

[5] Garnier, P., Abriou, D., & Gaudiot, J. J. (1988). *U.S. Patent No. 4,778,502*. Washington, DC: U.S. Patent and Trademark Office.

[6] H. Takana, J. Jang, J. Igawa, T. Nakajima, O.P. Solonenko, H. Nishiyama, Improvement of in-flight alumina spheroidization process using a small power argon DC-RF hybrid plasma flow system by helium mixture, J. Therm. Spray Technol. 20 (3) (2011) 432–439.

[7] W. Sexton, Porous wall, hollow glass microspheres, Savannah River National Laboratory Aiken, South Carolina 29808 (No. SRNL-L4130-2012-00004), SRS, 2012.

[8] A. Melling, Tracer particles and seeding for particle image velocimetry, Meas. Sci. Technol. 8 (12) (1997) 1406.

[9] D.L. Black, M.Q. McQuay, M.P. Bonin, Laser-based techniques for particle-size measurement: a review of sizing methods and their industrial applications, Prog. Energy Combust. Sci. 22 (3) (1996) 267–306.

[10] L. Gallo, V. Bucalá, M.V. Ramírez-Rigo, Formulation and characterization of polysaccharide microparticles for pulmonary delivery of sodium cromoglycate, AAPS Pharm. Sci. Technol. (2016) 1–12.

[11] T.M. Crowder, J.A. Rosati, J.D. Schroeter, A.J. Hickey, T.B. Martonen, Fundamental effects of particle morphology on lung delivery: predictions of Stokes' law and the particular relevance to dry powder inhaler formulation and development, Pharm. Res. 19 (3) (2002) 239–245.

[12] S.P. Newman, H.K. Chan, In vitro/in vivo comparisons in pulmonary drug delivery, J. Aerosol Med. Pulm. Drug Deliv. 21 (2008) 77–84.

[13] T. Srichana, G.P. Martin, C. Marriott, Dry powder inhalers: the influence of device resistance and powder formulation on drug and lactose deposition in vitro, Eur. J. Pharm. Sci. 7 (1) (1998) 73–80.

[14] M.J. Telko, A.J. Hickey, Dry powder inhaler formulation, Respir. Care 50 (9) (2005) 1209–1227.

[15] X. Kou, S.T. Wereley, P.W.S. Heng, L.W. Chan, M.T. Carvajal, Powder dispersion mechanisms within a dry powder inhaler using microscale particle image velocimetry, Int. J. Pharm. 514 (2) (2016) 445–455.

[16] W. Wong, D.F. Fletcher, D. Traini, H.K. Chan, J. Crapper, P.M. Young, Particle aerosolisation and break-up in dry powder inhalers 1: evaluation and modelling of venturi effects for agglomerated systems, Pharm. Res. 27 (7) (2010) 1367–1376.

[17] S.P. Rwei, I. Manas-Zloczower, D.L. Feke, Observation of carbon black agglomerate dispersion in simple shear flows, Polym. Eng. Sci. 30 (12) (1990) 701–706.

[18] U.T. Lieu, S. Harada, Stability of restructured non-fractal aggregates in simple shear flow, Adv. Powder Technol. 26 (3) (2015) 705–710.

[19] S. Takada, K. Saitoh, H. Hayakawa, Simulation of cohesive fine powders under a plane shear, Phys. Rev. E 90 (6) (2014) 062207.

[20] D. Saha, M.U. Babler, M. Holzner, M. Soos, B. Lüthi, A. Liberzon, W. Kinzelbach, Breakup of finite-size colloidal aggregates in turbulent flow investigated by three-dimensional (3D) particle tracking velocimetry, Langmuir 32 (1) (2015) 55–65.

[21] T.R. Sosnowski, K. Giżyńska, Ł. Żywczyk, Fluidization and break-up of powder particle aggregates during constant and pulsating flow in converging nozzles, Colloids Surf. A Physicochem. Eng. Asp. 441 (2014) 905–911.

[22] P.M. Gerde, Lovelace Respiratory Research Institute, Dust gun-aerosol generatorand generation. U.S. Patent 6,003,512 (1999).

[23] N.A. Buchmann, C.E. Willert, J. Soria, Pulsed, high-power LED illumination for tomographic particle image velocimetry, Exp. Fluids 53 (5) (2012) 1545–1560.

[24] M.J. McPhail, M.H. Krane, A.A. Fontaine, L. Goss, J. Crafton, Multicolor particle shadow accelerometry, Meas. Sci. Technol. 26 (2015), 045301.

[25] D. Bröder, M. Sommerfeld, Planar shadow image velocimetry for the analysis of the hydrodynamics in bubbly flows, Meas. Sci. Technol. 18 (8) (2007) 2513.

[26] J. Estevadeordal, L. Goss, PIV with LED: particle shadow velocimetry (PSV), 43rd AIAA Aerosp. Sci. Meet. Exhib., Meeting Papers January, 2005, pp. 12355–12364.

[27] H. Schlichting, Boundary layer theory. Part 2; turbulent flows, National Advisory Committee for Aeronautics Technical Memorandum No. 1218 1949, p. 65.

[28] E. Gutmark, I. Wygnanski, The planar turbulent jet, J. Fluid Mech. 73 (03) (1976) 465–495.

[29] C. Fureby, F.F. Grinstein, Large eddy simulation of high-Reynolds-number free and wall-bounded flows, J. Comput. Phys. 181 (1) (2002) 68–97.

[30] H. Sato, The stability and transition of a two-dimensional jet, J. Fluid Mech. 7 (1) (2006) 53–80.

[31] X. Lu, S. Yang, J.R. Evans, Studies on ultrasonic microfeeding of fine powders, J. Phys. D. Appl. Phys. 39 (11) (2006) 2444.

[32] Y.A. Cengel, J.M. Cimbala, Fluid mechanics: fundamentals and applications, second ed. McGraw Hill Publication, 2010 648–649.

[33] C. Willert, B. Stasicki, J. Klinner, S. Moessner, Pulsed operation of high-power light emitting diodes for imaging flow velocimetry, Meas. Sci. Technol. 21 (7) (2010) 075402.

[34] A.J. Susa, Investigation of Spray Formation Using LED Based High-speed, High-resolution Imaging(Doctoral dissertation) Univ. Wisconsin–Madison, 2016.

[35] D. Schulze, Flow properties of powders and bulk solids, Braunschweig/Wolfenbuttel, Univ. Appl. Sci, Germany, 2006.

[36] M.J. McPhail, A.A. Fontaine, M.H. Krane, L. Goss, J. Crafton, Correcting for color crosstalk and chromatic aberration in multicolor particle shadow velocimetry, Meas. Sci. Technol. 26 (2) (2015) 025302.

[37] G. Calvert, A. Hassanpour, M. Ghadiri, Mechanistic analysis and computer simulation of the aerodynamic dispersion of loose aggregates, Chem. Eng. Res. Des. 89 (5) (2011) 519–525.

[38] C. Weiler, M. Wolkenhauer, M. Trunk, P. Langguth, New model describing the total dispersion of dry powder agglomerates, Powder Technol. 203 (2) (2010) 248–253.

[39] G. Calvert, A. Hassanpour, M. Ghadiri, Analysis of aerodynamic dispersion of cohesive clusters, Chem. Eng. Sci. 86 (2013) 146–150.